Spatial proton exchange membrane fuel cell performance under carbon monoxide poisoning at a low concentration using a segmented cell system

Tatyana V. Reshetenko*, Keith Bethune, Richard Rocheleau

Hawaii Natural Energy Institute, University of Hawaii, 1680 East-West Road, POST 109, Honolulu, HI 96822, USA

HIGHLIGHTS

► The impacts of CO on PEMFC were studied with a segmented cell and spatial EIS.
► The experiments were done under galvanostatic control of overall cell current.
► Injection of 2 ppm CO resulted in a voltage decrease and redistribution of segments' currents.
► Inlet segments showed a decrease in current, downstream segments exhibited an increase in current.
► An increased membrane gas crossover can mitigate the impact of CO.

ARTICLE INFO

ABSTRACT

The impact of the fuel contaminant CO, which was intentionally injected in to the hydrogen stream at a concentration of 2 ppm, on proton exchange membrane fuel cell (PEMFC) performance distribution was studied using a segmented cell system and spatial electrochemical impedance spectroscopy (EIS). The cell was operated under a galvanostatic control of the overall cell current at 0.8 A cm^{-2}, and tests were carried out under H_2/O_2, H_2/air, and H_2/H_2 gas configurations. Upon CO injection the voltage decreased by 0.080, 0.300, and 0.320 V for O_2, air, and H_2 cathode gases, respectively. The voltage drop was accompanied by changes in the current density distributions. Inlet segments 1–4 showed a decrease in current due to CO adsorption on Pt, while, downstream segments 7–10 exhibited an increase in current. The performance completely recovered within 1–2 h after CO injection was stopped. The conversion of CO proceeds through a combination of catalytic and electrochemical oxidation reactions; however, the catalytic oxidation of CO is likely the dominant process. It was found that an increased membrane gas permeability can mitigate the impact of CO, mainly due to the catalytic oxidation of adsorbed CO on the Pt anode by the permeated O_2.

1. Introduction

Proton exchange membrane fuel cells (PEMFCs) have received significant attention in the last decade, as they are considered promising as power sources for electric vehicles, portable power units, or residential power systems [1–9]. Fuel cells convert chemical energy directly into electrical energy, making them highly efficient power sources with zero polluting emissions. A practical source for fueling PEMFCs is hydrogen produced via steam reforming or partial oxidation of natural gas [10,11]. In addition, several other processes must be employed to produce hydrogen pure enough to be used in PEMFCs, including desulfurization, the water gas shift reaction, and preferential oxidation. The last two processes minimize the CO content to less than 100 ppm. However, even low concentrations of CO lead to decreases in fuel cell performance and durability, mainly due to low operating temperatures (up to 80 °C) and the use of Pt as an electrocatalyst. For Pt-based electrodes 2–10 ppm of CO is enough to cause a drastic reduction in cell power [11–16]. Modifications of Pt catalysts by alloying with Ru have increased CO tolerances up to 100 ppm [15–17], and the further development of new catalysts is very promising. It is also possible to improve the CO removal process, and it is believed that CO at concentrations less than 200 ppb will result in acceptable PEMFC performance, even with Pt electrodes [18].

It is well known that the severe impact of CO occurs due to the higher affinity of Pt toward CO than toward hydrogen. As a result of this affinity most catalyst sites become occupied by CO, leading to

* Corresponding author. Tel.: +1 808 593 1714; fax: +1 808 593 1719.
 E-mail address: tatyanar@hawaii.edu (T.V. Reshetenko).

practically no current generating capability [12,16]. Thus, the operation of a cell with a reformate gas as a fuel likely causes a distribution of poisoned catalyst electrodes downstream. It creates specific areas of very low performance in the membrane electrode assembly (MEA), located mainly in the inlet of the cell, resulting in the redistribution of the local currents. Evaluation of fuel cell performance with a single cell approach only provides an average of local voltage, current, and impedance values and does not reveal the spatial behavior of the cell. A segmented cell system is a powerful tool for understanding the details of locally resolved fuel cell processes [19,20]. In general, segmented cell systems are divided into two separate classes: invasive and non-invasive [21]. Non-invasive approaches for the local electrochemical characterization of PEMFCs do not require any physical modifications of the components involved in the fuel cell assembly and are supported by sophisticated magnetic field measurement devices [22–24]. Invasive techniques require segmentation of one or several of the following components: current collector, bipolar plate, and gas diffusion layer (GDL). Invasive segmented cell systems are classified into four categories based on their current detection approaches: printed circuit board systems [25,26], resistor network systems [27–30], Hall sensors (open or closed loop) [31–37], and systems that use electronic load to control each individual segment voltage/current [27,38–42].

The Hawaii Natural Energy Institute's (HNEI) segmented cell approach for the study of PEMFCs was built on works of Cleghorn et al. [25], the German Aerospace Center, Stuttgart [31], Ballard Power Systems Inc. [27], and Los Alamos National Laboratory (LANL) [32]. HNEI's segmented cell system is partially based on the LANL design using closed loop Hall sensors and an improved data acquisition system. These enhancements allow the system to perform simultaneous rather than sequential measurements of spatial electrochemical impedance spectra (EIS), spatial linear sweep voltammetry (LSV), and cyclic voltammetry (CV).

There are many examples of segmented cell research applications, including the investigation of the local current distribution in a PEMFC [25–28,35,36,38,43,44], gas and water management [34,42,45,46], fuel cell stack diagnostics [26], and defect detection and localization [47–49]. However, there are only a few papers devoted to the study of current distributions with poisoned electrodes [50–53]. Authors [50] found current redistribution under CO poisoning at 100 ppm: the inlet part of the cell showed a decrease in performance while the outlet exhibited an increase. Distribution under CO poisoning at the anode was studied also in another paper [51]. Localized CO stripping measurements were obtained with a constant CO injection of $0.2\ cm^3$ at a carrier gas flow rate between 1 and $50\ cm^3\ min^{-1}$. The distribution of CO along the flow field was found to depend on diffusion within the GDL, CO uptake, the local level of CO coverage of the catalyst, and the exposure time: uneven distribution of the CO coverage was caused by low carrier gas flow rates. A heterogeneous distribution of CO likely leads to an uneven current distribution when power is drawn and reduces the initial fuel cell performance. However, the authors noted that under a high carrier gas flow rate the accumulation of CO was more homogeneous, which is beneficial to cell performance. The impacts of 10 and 80 ppm of CO on Pt/C and PtRu/C anodes under galvanostatic and potentiostatic controls were studied in another work [52]. The authors showed that in the case of the Pt/C anode the impact of CO on the performance was very significant. It was also mentioned that a steady state was reached within 60 min of CO exposure and the current at the inlet of the cell was lower than the current at the outlet. A recent paper [53] presented the poisoning effects of CO (1.5 and 3.0%) on a performance distribution of a high temperature PEMFC (160 and 180 °C) under galvanostatic and potentiostatic load control. The authors found a similar inhomogeneous current distribution trend when the fuel cell poisoning was evaluated in galvanostatic mode, as described previously [50–52]. Thus, there is a lack of work studying effects of low CO concentrations (less than 5 ppm) on spatial fuel cell responses despite the high importance of these results for determining fuel quality requirements. Moreover, no local impedance measurements in fuel cells under CO exposure have been reported thus far. The purpose of this paper was to investigate the impact of a low concentration of CO (2 ppm) on current distributions along flow field during different phases of exposure: beginning, steady state, and recovery. Local performance data are supported by analysis of spatial EIS measurements recorded under CO exposure.

2. Experimental

All experiments were conducted on a single cell test station using HNEI's segmented cell system, which enabled the simultaneous acquisition of spatially distributed data [43]. The segmented cell hardware was based on HNEI 100 cm^2 cell design. The hardware contains a segmented anode flow field consisting of ten consecutive segments disposed along the path of a ten channel serpentine flow field (Fig. 1a). Each segment has an area of 7.6 cm^2, has its own distinct current collector and GDL. The same channel designs were used for both the segmented anode and the standard cathode flow fields (reactant streams were arranged in a co-flow configuration). The hardware was operated with standard 100 cm^2 Ion Power MEAs. The anode and cathode electrodes were made with a 50% Pt/C catalyst coated on a DuPont™ Nafion® NRE212 membrane with a loading of 0.4 $mg_{Pt}\ cm^{-2}$. We used a Pt/C catalyst as a model system in this work because it shows a noticeable response even at low CO
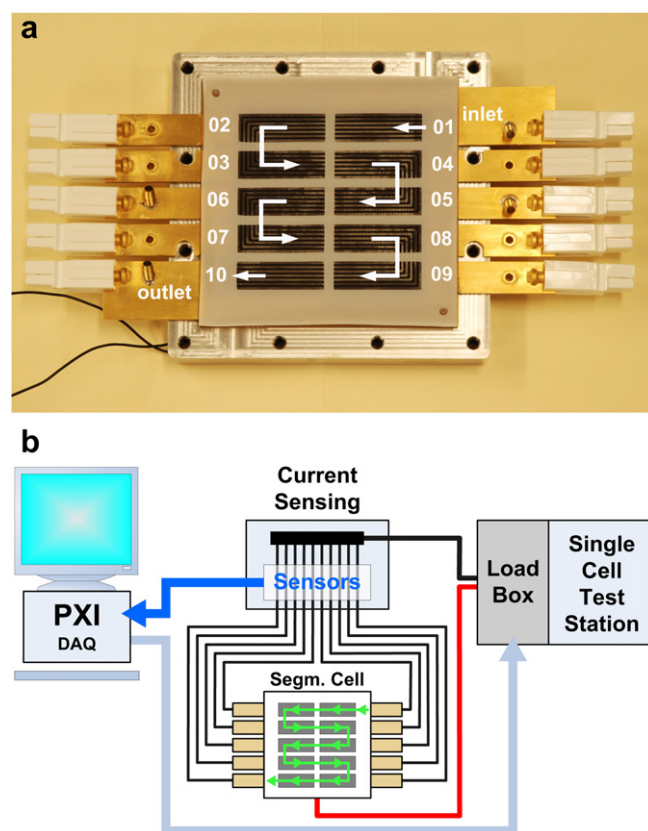

Fig. 1. Segmented anode hardware including gasket and current collector plate (a), and segmented cell measurement setup (b). Reprinted from Ref. [43], T.V. Reshetenko, G. Bender, K. Bethune, R. Rocheleau, Electrochim. Acta 56 (2011) 8700–8710, copyright (2011), with permission from Elsevier.

poisoning concentrations. The gasket material was made of Teflon®, with thicknesses of 203 μm and 178 μm for the anode and cathode, respectively. Sigracet® 25 BC was used as anode and cathode GDLs. The anode used a segmented GDL and gasket configuration, whereas a single GDL was applied at the cathode.

The segmented cell system consists of the cell hardware, the current transducer system, the data acquisition device, and a single cell test station (Fig. 1b). The current transducer system was custom designed. For current sensing, a closed loop Hall sensor device from Honeywell, Model CSNN191, was employed. The system allowed the interrogation of up to 10 current channels in a high (standard) and 16 channels in a low current mode. The standard current mode enabled the measurement of segment currents up to 15 A. The current limit of the data acquisition system can be extended to 30 A or more using a unique counter current technology that allows a flexible segmented cell design, high current operation, and increased accuracy during EIS experiments. The low current mode of the system yields a very accurate current measurement up to 375 mA, a convenient feature for CV or LSV experiments. Voltage and current signal data collection was performed with a National Instrument PXI data acquisition instrument operating on HNEI developed LabView programs. The data sampling frequency of the PXI system was 1 MHz, sufficient for measuring simultaneous responses from 10 segments. The segmented fuel cell was operated as a single cell in either voltage or current control mode using a standard fuel cell test station from Fuel Cell Technologies with current and power limitations of 240 A and 1.2 kW, respectively. Standardized single fuel cell testing protocols were applied while recording spatially resolved data using the segmented cell hardware and the data acquisition system. In this work the segments' currents and voltages and the cell voltage responses were recorded at a fixed overall cell current (galvanostatic control). Such operation minimized any impact from the segmented cell system and facilitated property distributions measurements without interference on the segments' performances (in plane currents). The system was designed such that the segments' voltages and cell voltage responses were the same (with a relatively small fuel cell active area). The operation of the segmented cell system was representative of real operating conditions, as only the overall current was controlled, while both segments' currents and voltages were floating.

During exposure the CO contaminant gas was intentionally injected at a concentration of 2 ppm into the humidified hydrogen, keeping the humidification of the gas constant by increasing the temperature setting of the humidifier unit. Anode/cathode testing conditions for the contamination experiments were H_2/air (H_2/O_2 and H_2/H_2), 48.3/48.3 kPa$_g$ backpressure, 100/50% relative humidity, and 2/2 stoichiometry. The cell temperature was 60 °C. The cell was operated under overall cell current of 0.8 A cm^{-2}. The contaminant experiment was divided into three phases, as described previously [54]:

- Phase 1 was a pre-poisoning period conducted with neat H_2 at the anode. The minimum length of Phase 1 was approximately 1/3 of the length of the entire experiment.
- Phase 2 was a poisoning period conducted with a constant amount of contaminant injected into the anode feed stream.
- Phase 3 was a recovery period conducted again with neat H_2/air.

The contamination experiment was also conducted in H_2/O_2 and in a driven H_2/H_2 mode. In the case of the H_2/H_2 test, the gas flow rate was 847 ml min^{-1}, and the relative humidities were 100% for both the anode and cathode. Cathode feed gas composition variations provided valuable data regarding the effects of O_2 concentration on anode poisoning by CO, a possible mechanism of the process, as well as potential mitigation strategies.

The polarization curves (VI curves) were measured at the same conditions as the contamination experiment. VI measurements were also performed in the H_2/O_2 configuration. In the latter case the same flow rates were used as in the H_2/air configuration to keep the water transport in and out of the cell identical at a given total cell current density. Consequently, the stoichiometry for O_2 increased to 9.5. The resulting two different VI curves (H_2/air and H_2/O_2) were used for the determination of a segment's activation, ohmic, and mass transfer overpotentials, as described previously [43].

The VI measurements and the contamination experiments were combined with EIS to determine the cell's and segments' high frequency resistances (HFR) and to measure the electrochemical impedance spectra for all ten segments and the overall cell. The selected frequency range for EIS experiments was 0.1 Hz–10 kHz, and the amplitude of the sinusoidal current signal perturbation was 2 A, which resulted in a cell voltage response of 10 mV or lower. The HFR was determined from the intercept of the EIS with the x-axis at higher frequencies at a Nyquist plot.

CV experiments were conducted for the determination of the electrochemical area (ECA) using a Parstat 2273 potentiostat/galvanostat from EG&G Instruments Corp. CVs were performed at a cell temperature of 35 °C with a scan rate of 20 mV s^{-1} while 100% humidified hydrogen and nitrogen were supplied to the reference/counter and working electrodes, respectively, at a flow rate of 750 ml min^{-1}. For each measurement, three cycles were applied over a potential range from −0.015 to 1.1 V vs. the hydrogen reference electrode (HRE). The hydrogen desorption peak area of the third cycle was used to determine the ECA. Hydrogen crossover experiments were performed at the same temperature and flow conditions as the ECA experiments using a single potential sweep from 0.1 to 0.4 V vs. the HRE at a scan rate of 0.1 mV s^{-1}.

Prior to the CO exposure experiment the segmented cell was assembled using established procedures, conditioned, and subjected to a set of beginning diagnostic tests. The diagnostics consisted of CV to determine the ECAs of the electrodes, LSV to find the hydrogen crossover current of the cell, and the measuring of VI curves with spatial EIS using H_2/air and H_2/O_2 gas configurations to determine the performance, overpotential distributions of the cell, and impedance responses. The same set of diagnostic tests was repeated after the CO experiment. A comparison of the results before and after the CO
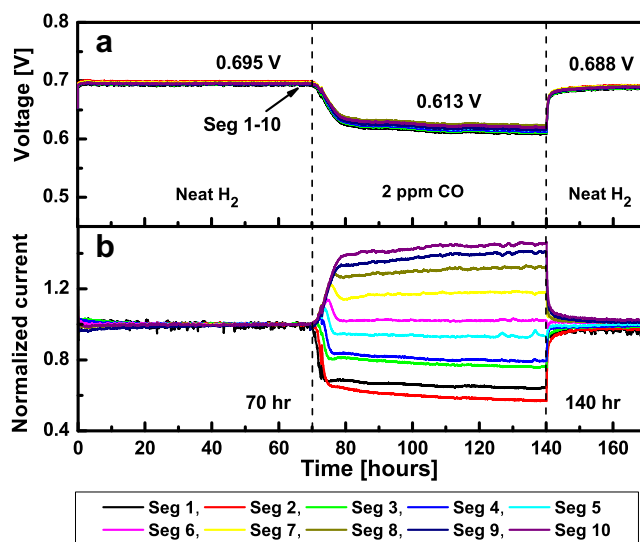

Fig. 2. Voltages (a) and current densities of each segment normalized to its initial performance (b) vs. time for an overall current density of 0.8 A cm^{-2} and contaminant exposure to 2 ppm CO. Anode/cathode: H_2 + 2 ppm CO/O_2, 2/2 stoichiometry, 100/50% RH, 48.3/48.3 kPa$_g$, 60 °C.

exposure provided insights into the impacts of the contaminant on the spatial properties of the cell. The same MEA sample was used for three CO exposure tests carried out at different gas configurations: H_2/O_2, H_2/air, and H_2/H_2. The MEA was reconditioned after each test.

3. Results and discussion

3.1. Performance under CO exposure at H_2/O_2 operating conditions

Measurements performed with H_2 + 2 ppm CO/O_2 were carried out in the galvanostatic mode at a constant overall cell current of 0.8 A cm^{-2}. Fig. 2 shows the voltage responses and current densities of each segment normalized to its initial performance vs. experiment time for all ten segments. A pre-poisoning period was conducted with neat H_2 for the first 70 h. The segments' voltages and the overall cell voltage were 0.695 V due to the design of the segmented cell system and the small sizes of the electrodes and the

cell. Operation with pure O_2 results in a relatively homogeneous current density distribution along the flow field. The individual segments' performances were stable during the pre-poisoning phase, which was confirmed by spatial EIS data.

Fig. 3 presents impedance spectra for all ten segments and the overall cell during different phases of the experiment. Fuel cell impedance spectra without CO poisoning included several arcs: a high frequency anode arc (usually this arc is relatively negligible but sometimes it is visible at low current densities), a high frequency cathode arc attributed to a charge transfer resistance and double layer capacitance within the cathode catalyst layer, and a low frequency arc reflecting mass transfer limitations in the gas and ionomer phases within the GDL and the cathode catalyst layer [55]. The membrane itself is resistive due to a limited proton transport rate, which, in combination with the electronic contact resistance, determines the MEA HFR. A comparison of the EIS curves recorded at the pre-poisoning phase (69 h) shows that all
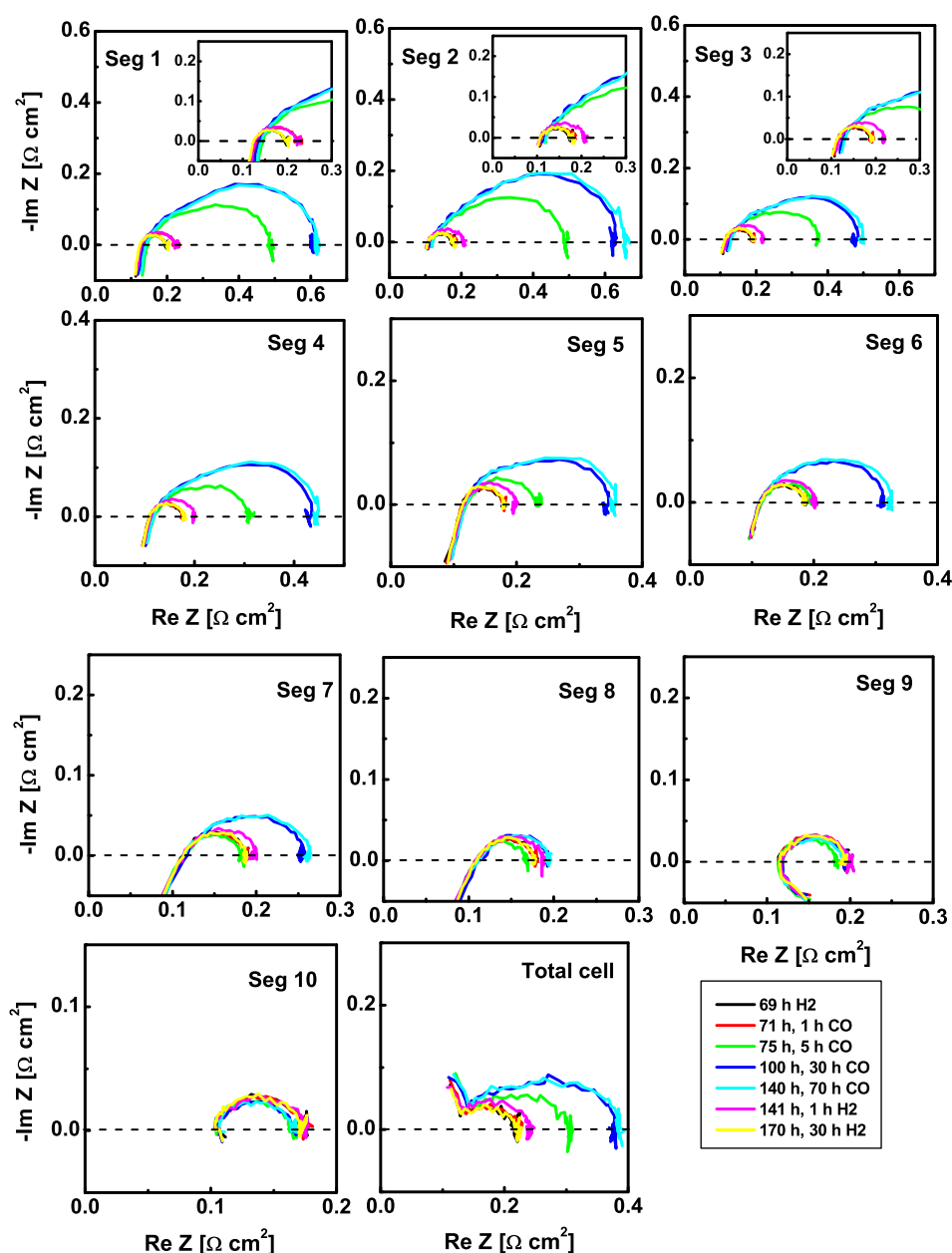

Fig. 3. Electrochemical impedance spectra for segments 1–10 and the total cell during different CO exposure phases (2 ppm). Anode/cathode: H_2/O_2, 2/2 stoichiometry, 100/50% RH, 48.3/48.3 kPa$_g$, 60 °C, 0.8 A cm^{-2}.

segments had similar impedances (Fig. 3). There are a small anode and significant cathode impedance semicircles. A low frequency arc responsible for mass transfer limitations was not observed under operation with pure O_2.

Immediately after the injection of 2 ppm CO into the H_2 stream transition behavior — a fast decrease in the segments' voltages and redistributions of the current densities — was observed within the first 10 h (Fig. 2). Subsequently, the segments reach steady state, when the current densities and voltages are stable. The segments' voltages at the steady state were 0.613 V, with the voltage drop reaching 0.080–0.085 V. Under pure hydrogen operation, current densities varied between 0.76 A cm^{-2} (segment 1) and 0.80 A cm^{-2} (segment 9); when pure hydrogen was replaced by hydrogen containing 2 ppm CO, a maximum current density of 1.16 A cm^{-2} was found in segment 10 and a minimum density of 0.50 A cm^{-2} was observed for segments 1 and 2. Under CO exposure inlet segments 1–4 were characterized by lower current densities than outlet segments 7–10 due to the adsorption of CO at the inlet part of the cell and the reduction of the CO concentration downstream. The same current density redistribution behavior under the gal-vanostatatic mode was observed in previous papers [52,53]. However, it was reported [53] that operation under potentiostatic control of the cell did not result in such drastic current redistributions: the current density distribution after CO injection was nearly the same as the initial distribution.

The evolutions of the segments' impedance responses are shown at Fig. 3. After 1 h of CO injection there was a slight increase in impedance for segment 1, while the others did not show any changes. Segments 1–5 exhibited increases in impedance after 5 h of CO exposure. The injection of CO over 30 h resulted in changes in the EIS curves for segments 1–7 corresponding to the steady states of the segments and of the cell. However, there were no changes in EIS for segments 8–10, and the impact of CO on the outlet segments was negligible due to CO consumption by catalyst upstream and cell operation with pure O_2. It should be noted that we did not observe any pseudo-inductive loop at the low frequency range. The impedance of the total cell showed the same trend as the

impedances of the inlet segments. EIS curves of the total cell had pure inductances at very high frequencies, which may be due to inductance from wires and the size of the cell. This phenomenon was observed previously [56].

It was assumed that the alterations in the impedance spectra were dominated by changes in the anodic reactions. A separation of the anodic and the cathodic contributions is the main problem for analysis of the impedance spectra of a fuel cell, but the application of equivalent electrical circuits (EECs) allows us to gain insight into the processes at the electrodes (Fig. 4). Both electrodes consist of a porous system separated by the membrane, denoted as the electrolyte resistance (R_S). The impedance of the cathode is represented using charge transfer resistance ($R_{ct,O2}$) in parallel to a constant phase element (CPE$_{dl,c}$) and finite length Warburg diffusion element (W). Using pure O_2 as an oxidant eliminates the Warburg element in the EEC. In the case of neat H_2 operation, the anode is simulated by the anode charge transfer resistance ($R_{ct,H2}$) in parallel with double layer capacitance ($C_{dl,a}$) (Fig. 4a and c). However, the anode impedance is more complicated during CO exposure due to additional reactions involving CO adsorption and oxidation at the surface of the electrocatalyst. The effects of poisoning with CO are quantitatively described by the simplified model given in Fig. 4b and based on the models suggested by Wagner et al. [57], Chakraborty et al. [58], Liu et al. [59], and F. Hajbolouri [60]. This EEC represents the impedances of electrochemical reactions with single adsorbed intermediate where the diffusion of the participating species is not rate limiting. The anodic impedance is modeled by the double layer capacity ($C_{dl,a}$) in parallel with the Faraday impedance (Z_F). The Faraday impedance is the surface relaxation impedance, and it explains the development of the pseudo-inductive behavior in the low frequency range of the impedance spectra (up to 0.01 Hz) [57,61]:

$$Z_F = \frac{R_{ct,H2} + Z_C}{1 + R_{ct,H2}/Z_K}$$

In our case, Z_C was a finite diffusion impedance, and $Z_C = 0$ due to the assumption that there was no diffusion limitation of
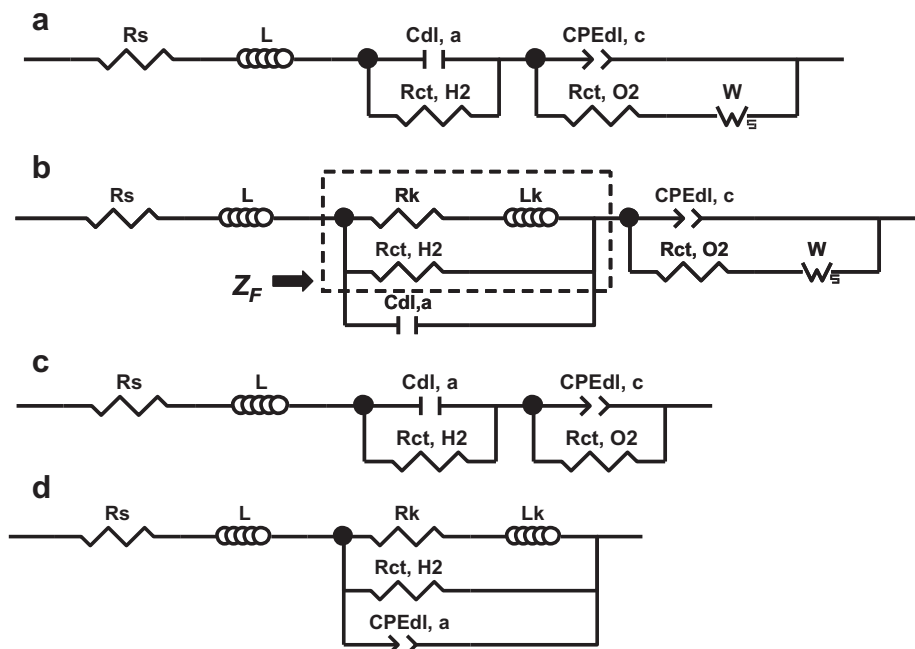

Fig. 4. Electrical equivalent circuit for H_2/air (a), during CO anode poisoning under H_2/air operation (b), under H_2/O_2 operating conditions with and without CO poisoning (c), and for the driven H_2/H_2 mode under CO exposure (d).

participating species at the anode, corresponding to the EEC suggested previously [60]. The Faraday impedance might be presented by a combination of the anode charge transfer resistance ($R_{ct,H2}$) and the relaxation impedance (Z_K). Z_K can be split into the relaxation resistance R_K and the relaxation inductivity X_K, with the pseudo-inductance $L_K = \tau_K R_K$, which is proportional to the relaxation time constant τ_K [57].

However, CO poisoning under H_2/O_2 operation results in the elimination of the Warburg element at the cathode circuit, and the absence of a pseudo-inductive loop at the low frequency region allows us to simplify the anode circuit and to consider the anode as only the charge transfer resistance in parallel to the double layer capacitance (Fig. 4c). In H_2/H_2 mode, the EEC can be presented as shown in Fig. 4d.

Fig. 5 presents the results of EEC modeling of the EIS curves for segment 1 under different operating conditions. The EEC shown at Fig. 4c was used for fitting the impedance spectra obtained at 2 ppm CO + H_2/O_2 configuration. In the case of air as an oxidant EIS data observed under CO poisoning were fitted using the EEC presented in Fig. 4b, while the EEC presented in Fig. 4d was applied to the EIS results obtained for 2 ppm CO + H_2/H_2. It is clear that the proposed EECs adequately described the experimental EIS curves, and our further publication will be devoted to a detailed analysis of the EIS data of a PEMFC poisoning by CO. With respect to the EIS data obtained under H_2/O_2 (Fig. 3), increases in the HFR and the anode charge transfer resistance as well as a slight increase in the cathode charge transfer resistance under CO exposure were observed [57], which is confirmed by the results of the EEC modeling for segment 1 (Fig. 5d). The changes in the impedance were dominated by the changes at the anode electrode; however, the changes at the cathode should also be taken into account. The effective charge transfer resistance is influenced by the concentrations of the charged and uncharged species (H_2O). The poisoning of the anode causes a local inhomogeneous distribution of the generated H^+ and a resulting inhomogeneous distribution of protonated and associated water molecules at the anode electrode
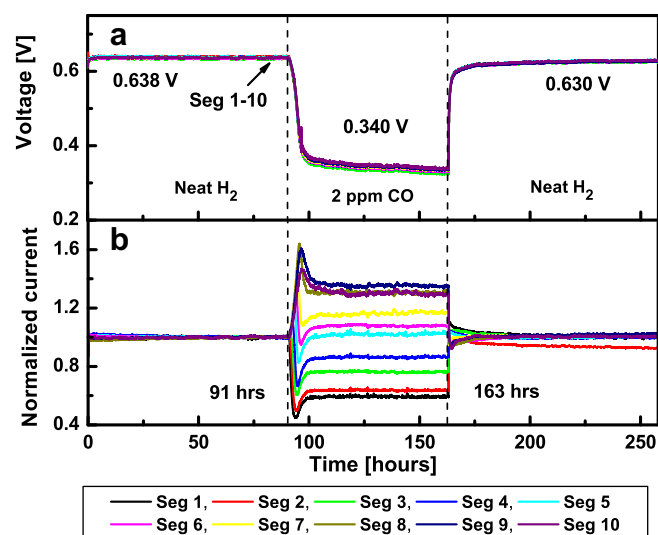

Fig. 6. Voltages (a) and current densities for each segment normalized to its initial performance (b) vs. time with an overall current density of 0.8 A cm^{-2} and a contaminant exposure of 2 ppm CO. Anode/cathode: H_2 + 2 ppm CO/air, 2/2 stoichiometry, 100/50% RH, 48.3/48.3 kPa$_g$, 60 °C.

and membrane. It also creates an uneven distribution of these species at the cathode, which leads to an increase in the cathode charge transfer resistance [57]. Moreover, it is possible to assume that there is also a diffusion of CO from the anode to the cathode [62], resulting in the poisoning of the cathode and an increase in $R_{ct,O2}$. After switching fuel from H_2 + 2 ppm CO to neat H_2 the cell and segment voltages immediately recovered to almost their initial values of 0.688 V (vs. 0.695 V). EIS curves after 1 h of recovery showed significant decreases in the segments' impedances. After several hours of recovery impedances of the segments and the total cell were very close to their initial values.
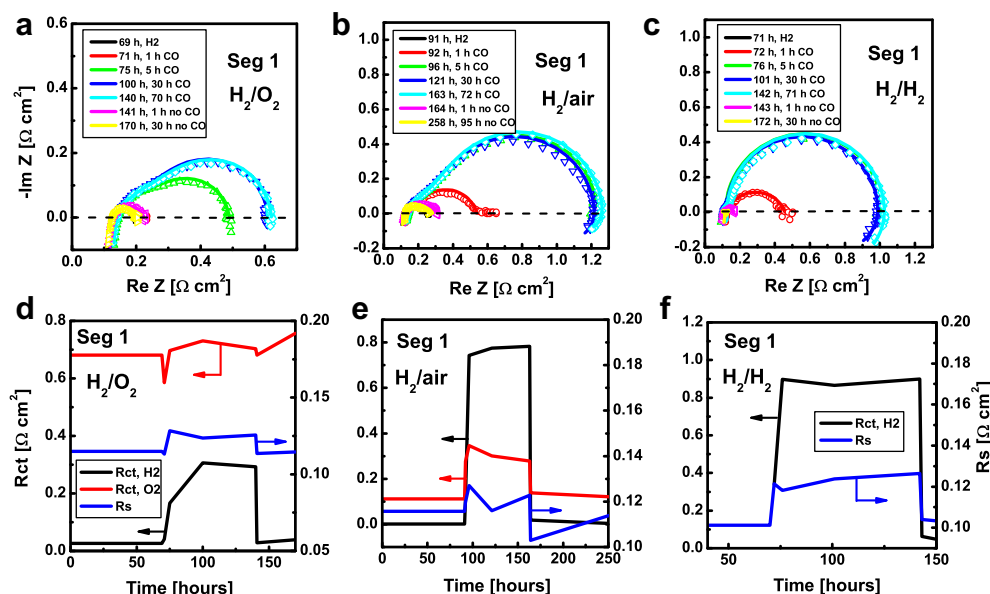

Fig. 5. EIS of segment 1 recorded for a total cell current density of 0.8 A cm^{-2} under different gas configurations: H_2/O_2 (a), $H_2/$air (b), and H_2/H_2 (c). The modeled results are represented with a solid line, and the experimental results are presented with similarly colored symbols. The evolution of serial resistance (R_s), anode and cathode charge transfer resistances ($R_{ct,H2}$ and $R_{ct,O2}$) for segment 1 under H_2/O_2 (d), $H_2/$air (e), and H_2/H_2 (f). Anode/cathode: H_2/O_2 (or air), 2/2 stoichiometry, 100/50% RH, 48.3/48.3 kPa$_g$, 60 °C. In the case of H_2/H_2 driven mode, anode/cathode: H_2/H_2, 0.847/0.847 l min^{-1}, 100/50% RH, 48.3/48.3 kPa$_g$, 60 °C. (For interpretation of the references to color in this figure legend, the reader is referred to the web version of this article.)

3.2. Performance under CO exposure at H_2/air operating conditions

Fig. 6 presents voltage responses and normalized current densities vs. experiment time for all ten segments under H_2/air operation. A pre-poisoning period was conducted with pure H_2 for the first 91 h. The segments' voltages and the overall cell voltage were 0.638 V. It should be noted that at H_2/air and with an overall current density of 0.8 A cm^{-2}, there were segment current distributions downstream: the current density for segment 1 was 0.88 A cm^{-2}, while the current density for segment 10 was 0.73 A cm^{-2}. At this current density the outlet segments operate under diffusion control of the reaction and suffer from water flooding as well as low O_2 partial pressure in the gas stream [43–45]. Such performance distribution at the pre-poisoning step was confirmed by spatial EIS. Impedance spectra for all ten

segments and the total cell at different phases of the test are presented in Fig. 7. A comparison of the curves recorded under neat H_2 shows the existence of a small high frequency anode loop, a cathode loop, and a low frequency arc, corresponding to mass transfer limitations. There was an increase in the diameter of the low frequency loop from the inlet to the outlet, reflecting growing diffusion limitation downstream.

The injection of 2 ppm CO into the H_2 stream results in a fast decrease in the segments' voltages and current redistributions (Fig. 6). After 5–7 h the cell reached a steady state with a voltage of 0.340 V, and the voltage drop was 0.295–0.3 V. The current densities of inlet segments 1–4 were lower than those of outlet segments 7–10: the current densities were 0.52 A cm^{-2} and 0.96 A cm^{-2} for segments 1 and 10, respectively. The evolutions of the segments' EIS are shown in Fig. 7. There was an increase in
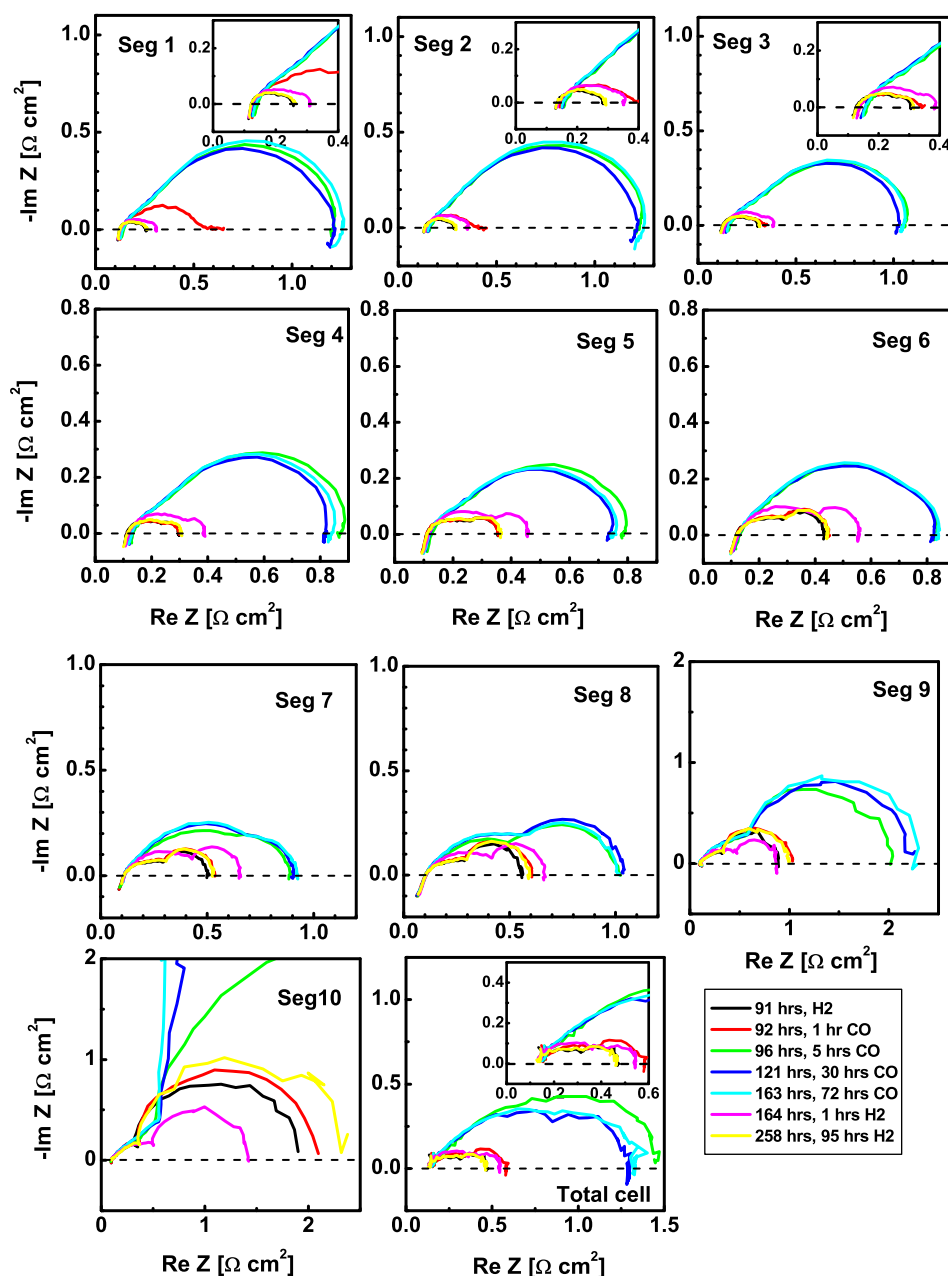

Fig. 7. Electrochemical impedance spectra for segments 1–10 and the total cell during different CO exposure phases (2 ppm). Anode/cathode: H_2/air, 2/2 stoichiometry, 100/50% RH, 48.3/48.3 kPa$_g$, 60 °C, 0.8 A cm^{-2}.

impedance for segments 1–3 after 1 h of CO exposure, while the others did not have any significant changes. Such changes are attributed to progressive CO poisoning of the catalyst at the inlet segments during the first hours of the CO injection. The catalyst poisoning is also accompanied by a reduction of the electrochemical reaction rate and the current produced, so the current density of the inlet segments decreases significantly. Because the cell was operated under the galvanostatic control and the overall cell current was kept constant, there were current increases in the outlet segments to compensate for the losses at the inlet segments.

Based on the EIS data, segments 1–6 reached steady state after 5 h of CO injection. There were increases in the anode, cathode loops, and HFR for the inlet segments. Additionally, segments 1–4 had pseudo-inductive loops in the low frequency region. Segments 7–9 reached steady states several hours later. EIS curves of segments 1–9 after 30 h of 2 ppm CO exposure were identical to the curves after 72 h of CO exposure. The EEC depicted in Fig. 4b fully describes the electrochemical processes taking place at the anode and cathode at this current density under 2 ppm CO + H_2/air. From EIS data (Fig. 7), it is possible to conclude that under CO exposure there are increases in anode and cathode charge transfer resistances as well as in cathode Warburg resistance and in HFR, which is also confirmed by preliminary EEC modeling for segment 1 (Fig. 5b and e). The inductive behavior of segments 1–4 proves the existence of the slow process of CO oxidation involving at least one intermediate. However, segment 10 exhibited an increasing low frequency loop, which finally became negative and was located in quadrant II of the Nyquist plot (Fig. 7). Analysis of the segments' EIS reveals that the anode and cathode charge transfer resistances decreased downstream, and the impact of CO on the outlet segments became smaller due to the consumption of CO by previous segments and the reduction of CO concentrations downstream. The effect of CO on segment 10 was, therefore, probably negligibly small, and it's EIS behavior may be explained by mass transfer limitations and O_2 depletion [45] instead of CO poisoning [63,64]. After changing the anode gas from the H_2 + 2 ppm CO mixture to pure H_2, the cell segments' voltages recovered to 0.630 V and the segments' currents became similar to the initial values. EIS curves after 1 h of recovery demonstrated significant decreases in the segments' impedances, and the curves nearly returned to their initial states after several hours of recovery.

3.3. Performance under CO exposure at H_2/H_2 operating conditions

Voltage responses and normalized current densities vs. test time for all segments in the case of driven H_2/H_2 operation are presented in Fig. 8. During the pre-poisoning phase the segments' voltages were 0.110 V. After CO injection the anode potential increased and the voltage became 0.430 V, with a voltage difference of 0.320 V. The current density behavior was similar to the previous cases with H_2/O_2 and with H_2/air. For pure hydrogen operation current density distributions were in the range of 0.91 (segment 1) to 0.75 A cm^{-2} (segment 10). The injection of 2 ppm CO resulted in a decrease in the current densities of the inlet segments (0.53 A cm^{-2} for segment 1) and an increase for the outlet segments (1.27 A cm^{-2} for segment 10). The outlet segments had to increase their currents to keep the same overall current density. Fig. 9 shows spatial EIS data. CO exposure within 1 h led to an increase of the impedances of segments 1–3, while after 5 h the segments were at the steady state. The impendence spectra of segments 1–10 have a negligible high frequency arc and significant semicircle, corresponding to the processes at the anode: H_2 oxidation in the presence of CO and CO adsorption/oxidation. Additionally, there is a pseudo-inductive loop for segments 1–4. The impedance behavior at these
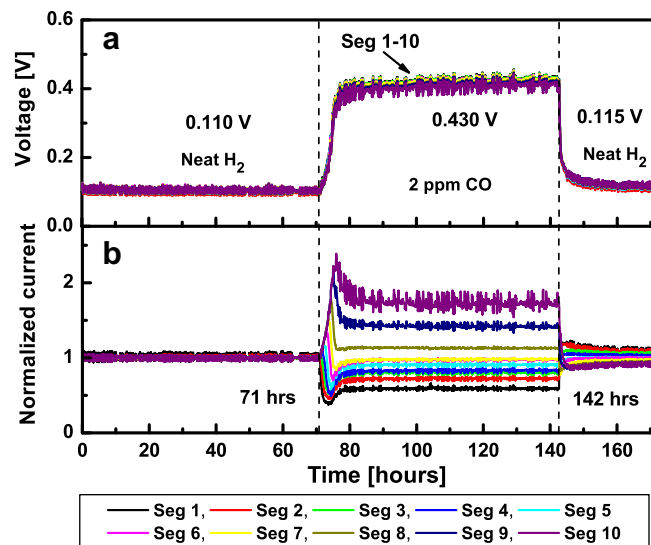

Fig. 8. Voltages (a) and current densities of each segment normalized to its initial performances (b) vs. time for an overall current density of 0.8 A cm^{-2} and a contaminant exposure of 2 ppm CO. Anode/cathode: H_2 + 2 ppm CO/H_2, 0.847/0.847 l min^{-1}, 100/100% RH, 48.3/48.3 kPa$_g$, 60 °C.

operating conditions can be described by the anode EEC depicted in Fig. 4d. It should be noted that EIS curves recovered very quickly after changing from the H_2 + 2 ppm CO mixture to pure H_2, as did the segments' voltages and current densities (Figs. 8 and 9).

3.4. Effect of CO exposure on electrochemical properties of the MEA

Fig. 10a–c present voltage distributions at fixed current densities as functions of the segment locations before and after the CO exposure tests carried out at the different gas configurations: H_2/O_2, H_2/air, and driven H_2/H_2. A comparison of the curves showed that, after the first CO exposure test under H_2/O_2 conditions, the performance did not change significantly (Fig. 10a). There was a slight decrease in the performances (0.020–0.025 V) of inlet segments 1–2 at low current densities (0.1–0.6 A cm^{-2}), while the performances increased for the outlet segments at high current densities. Fig. 10b shows voltage distributions before and after the second CO exposure test under H_2/air. The curves indicate that after the second CO test there was a slight performance decrease (0.020–0.030 V) in inlet segments 1–4, while the others had the same performances. An analysis of the segments' performances before and after the third CO test (H_2 + 2 ppm CO/H_2) reveals a slight decrease in the performances of the inlet segments (0.020 V) at low current densities and a decrease in the performances of segments 9 and 10 (0.020–0.050 V) over the entire current range (Fig. 10c).

After the CO poisoning at H_2/O_2 operating conditions a decrease of the overall cathode ECA was 9.38%, while the anode ECA drop was only 1.90%. Distributions of the anode and cathode ECA differences are shown in Fig. 10d. There was a slight decrease in the anode ECA for all segments (less than 1 m^2 g^{-1}). The cathode ECA distribution exhibited a surface area drop of 5–10 m^2 g^{-1}, and the outlet segments experienced more area loss than the inlet segments. After the first CO test (H_2/O_2), there was no pinhole formation in the MEA and the overall hydrogen crossover current was 0.59 mA cm^{-2}.

Fig. 10e presents data about the evolution of ECA after the 2 ppm CO + H_2/air test. The overall cathode ECA did not change, while the overall anode ECA decreased by 7.49%. The distribution of the anode
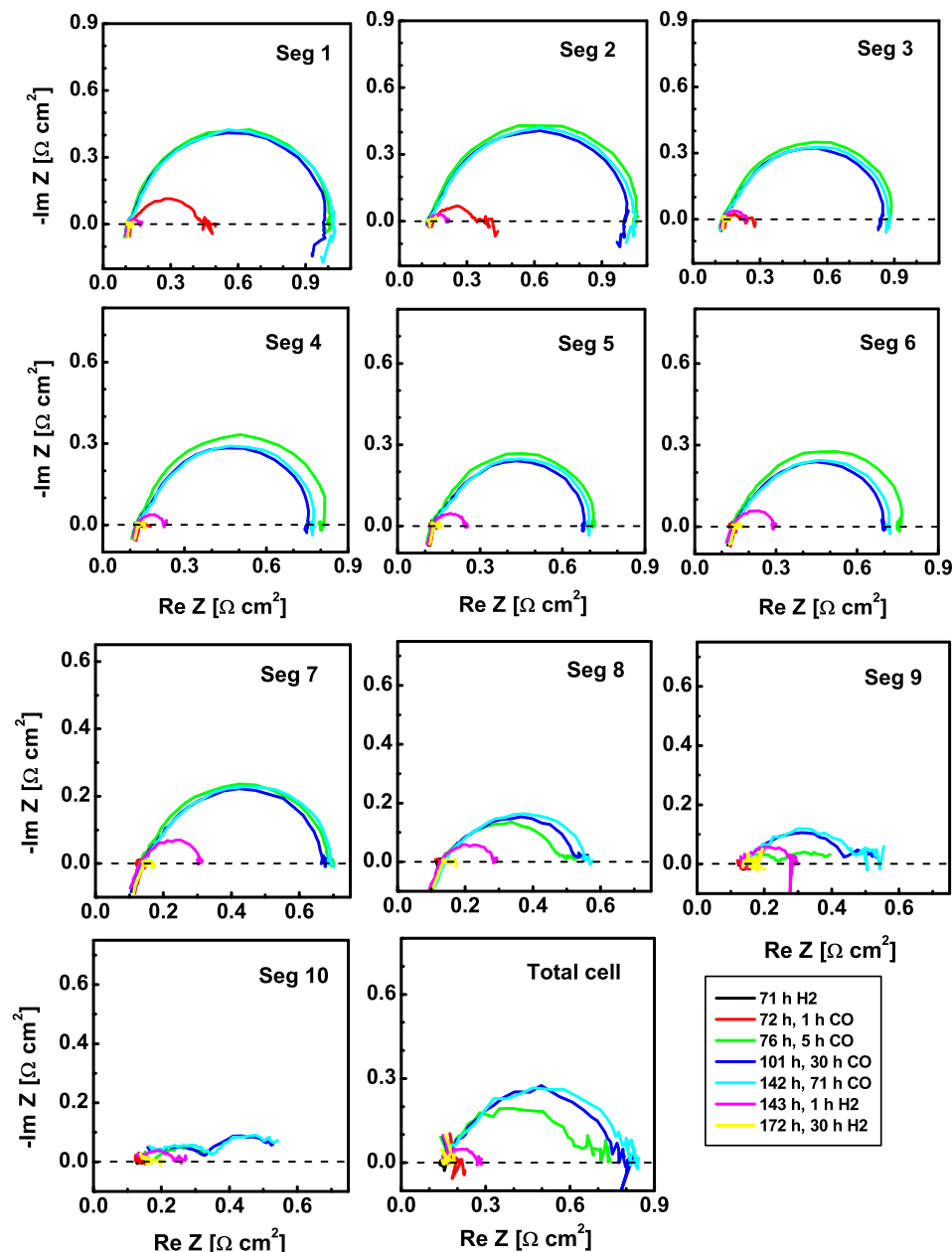
Fig. 9. Electrochemical impedance spectra for segments 1–10 and the total cell during different CO exposure phases (2 ppm). Anode/cathode: H_2/H_2, 0.847/0.847 l min^{-1}, 100/100% RH, 48.3/48.3 kPa$_g$, 60 °C, 0.8 A cm^{-2}.

ECA difference demonstrates a decrease in the anode ECA for all segments: the surface area dropped by ∼5 m^2 g^{-1}, and the outlet segments experienced more area loss than the inlet segments. After the CO test there was no pinhole formation in the MEA and the overall hydrogen crossover current was 0.61–0.62 mA cm^{-2}.

The effects of CO exposure at H_2/H_2 driven test conditions on ECA are shown in Fig. 10f. The overall cathode ECA slightly decreased (4.45%), while the total anode ECA decreased by 16.01%. The distribution of the anode ECA difference demonstrates a progressive decline in the ECA downstream, and the ECA drop for segment 10 was 30 m^2 g^{-1}. After the CO test there was no pinhole formation in the MEA and the overall hydrogen crossover current was 0.61 mA cm^{-2}. The observed performance decrease and the ECA decrease can be attributed to the degradation of the MEA and its components during the long term tests.

3.5. H_2 crossover effect on CO poisoning

During this study two MEAs were tested. Their main parameters are presented in Table 1. It was found that these samples had nearly the same anode and cathode ECAs. However, the overall H_2-crossover current for MEA 2 was 1.61 mA cm^{-2} vs. 0.61 mA cm^{-2} for MEA 1. It should also be noted that the performances of these samples were close (Fig. 11). At low current densities, the MEA 2 performance was slightly higher than that of MEA 1, but the opposite trend was observed at high current densities, and MEA 1 had a more homogeneous distribution. At 0.8 A cm^{-2}, the voltage of MEA 2 was 0.638 V, which is close to the 0.635 V observed for MEA 1.

Fig. 12 presents the segment 1 anode overpotential transients ($\Delta\eta_{anode}$) for both MEA samples, which were calculated according
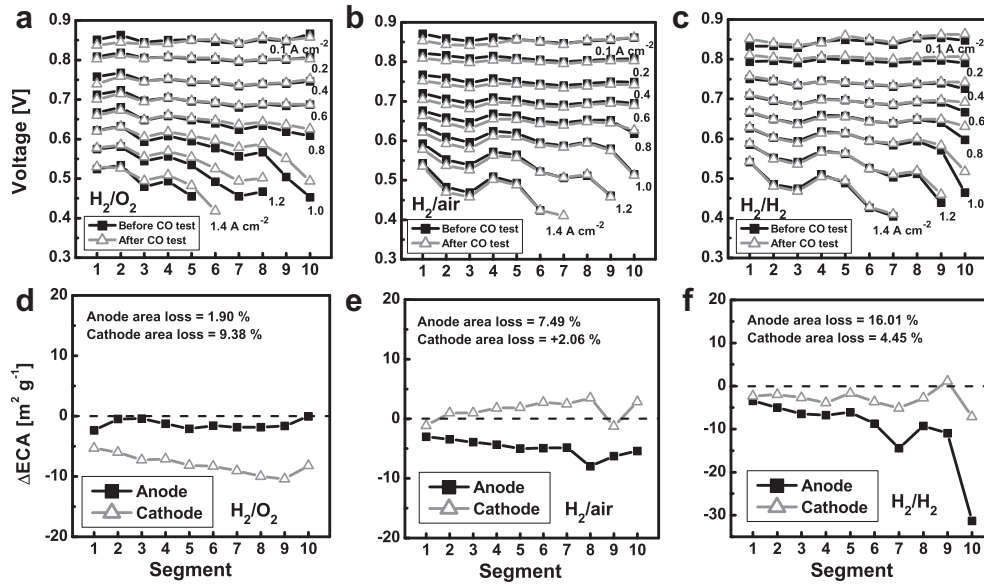
Fig. 10. Distributions of electrochemical properties. Cell voltage distribution for various current densities up to 1.4 A cm^{-2} before and after exposure to 2 ppm CO and O$_2$ (a), air (b), and H$_2$ (c) as oxidants. Anode/cathode for performance measurements: H$_2$/air, 2/2 stoichiometry, 100/50% RH, 48.3/48.3 kPa$_g$, 60 °C. Anode and cathode ECA differences between after and before CO exposure tests carried out with O$_2$ (d), air (e), and H$_2$ (f) as oxidants. Anode/cathode parameters for ECA: H$_2$/N$_2$, 0.75/0.75 l min^{-1}, 100/100% RH, 0/0 kPa$_g$, 35 °C, 20 mV s^{-1}.

to a reported method [54]. A significant anode overpotential difference was evident, with absolute values of 0.295–0.300 V and 0.210–0.215 V for MEA 1 and MEA 2, respectively. The differences in MEA behavior are ascribed to the differences in H$_2$-crossover. The MEA 1 is less permeable to H$_2$ and by extension to O$_2$, leading to a larger overpotential [65].
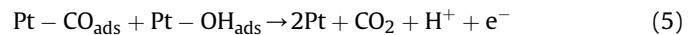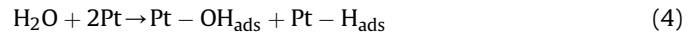
The observed impact of hydrogen crossover is supported by the anode overpotential data obtained for H$_2$/H$_2$, H$_2$/air, and H$_2$/O$_2$ tests. Anode overpotentials depended on the partial O$_2$ pressures at the cathode compartments (Fig. 13). Under H$_2$/O$_2$ gas configuration the anode overpotential was 0.075 V, and a decrease in the O$_2$ concentration (up to 21 vol.%) led to an increase in the anode overpotential to 0.295 V. The anode overpotential was at its highest during operation in the driven H$_2$/H$_2$ mode (0.315 V). Operation with pure O$_2$ on the cathode significantly mitigated the impact of the contaminant (Figs. 2 and 6).

There is still considerable controversy regarding the CO oxidation mechanism in fuel cells. In general, the oxidation of CO to CO$_2$ can occur via chemical and electrochemical pathways, or even a combination of both. The electrooxidation involves a surface reaction between adsorbed CO molecules and an oxygen containing species as it is presented in Equations (1) and (2) [13,14,66–70].

$$CO + Pt \leftrightarrow Pt - CO_{ads} \tag{1}$$

$$Pt - CO_{ads} + H_2O \rightarrow Pt + CO_2 + 2H^+ + 2e^- \tag{2}$$
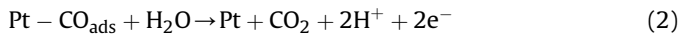
The water molecule acts as the oxygen source. However, the physical state of the oxygen-containing species is still uncertain. Presumably, H$_2$O molecules (or OH$^-$) adsorb on Pt, as shown in

Equations (3) and (4), and participate in the electrochemical oxidation of CO (Equations (2) and (5)).

$$H_2O + Pt \rightarrow Pt - H_2O_{ads} \tag{3}$$

$$H_2O + 2Pt \rightarrow Pt - OH_{ads} + Pt - H_{ads} \tag{4}$$

$$Pt - CO_{ads} + Pt - OH_{ads} \rightarrow 2Pt + CO_2 + H^+ + e^- \tag{5}$$

Oxygen diffusing from the cathode to the anode through the membrane provides a chemical rather than an electrochemical CO oxidation. This non-electrochemical mechanism was proposed by Zhang et al. [65] and is presented in Equations (6) and (7). In general, it is very similar to the preferential oxidation reaction, where adsorbed oxygen atom reacts with adsorbed CO. Another
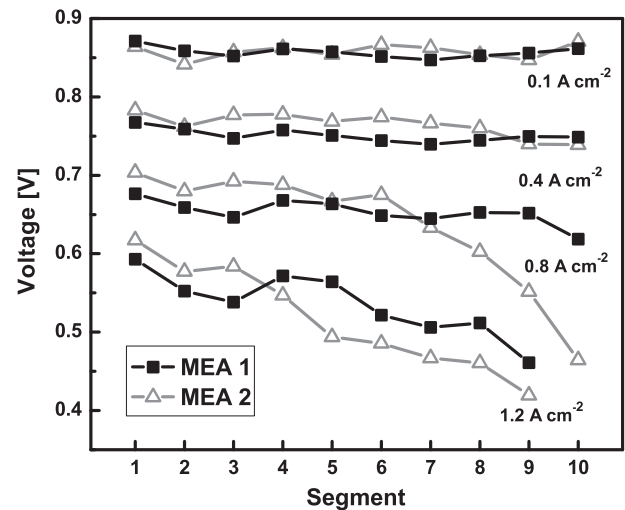

Fig. 11. Cell voltage distributions for various current densities up to 1.2 A cm^{-2} for the two MEA samples before the H$_2$ + 2 ppm CO/air test. Anode/cathode: H$_2$/air, 2/2 stoichiometry, 100/50% RH, 48.3/48.3 kPa$_g$, 60 °C.

Table 1
Initial electrochemical parameters of the two MEAs investigated.

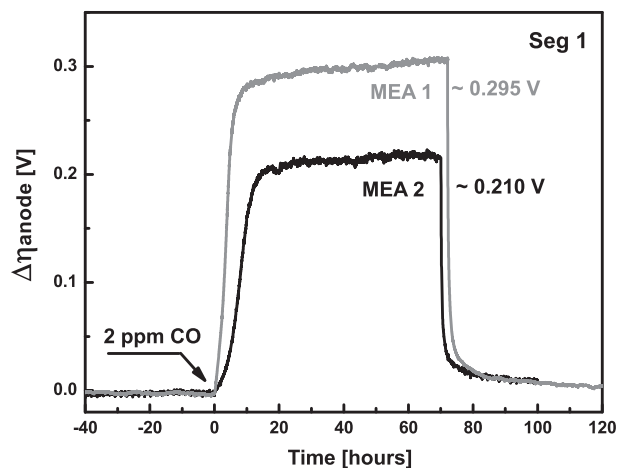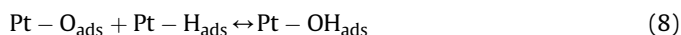| Sample	H$_2$-crossover [mA cm^{-2}]	ECA anode [m^2 g^{-1}]	ECA cathode [m^2 g^{-1}]	Voltage at 0.8 A cm^{-2} [V]
MEA 1	0.61	65.58	71.27	0.638
MEA 2	1.16	67.70	67.64	0.635

Fig. 12. Segment 1 transient anode overpotentials for both MEA 1 and 2 samples for an overall cell current of 0.8 A cm^{-2} and a 2 ppm CO exposure. Anode/cathode: H_2/air, 2/2 stoichiometry, 100/50% RH, 48.3/48.3 kPa$_g$, 60 °C.

possibility is that adsorbed O reacts with adsorbed H to form adsorbed hydroxyls (OH_{ads}) (Equation (8)), which electrochemically may react with adsorbed CO (Equation (5)).

$$O_2 + 2Pt \leftrightarrow 2Pt - O_{ads} \tag{6}$$

$$Pt - O_{ads} + Pt - CO_{ads} \rightarrow 2Pt + CO_2 \tag{7}$$

$$Pt - O_{ads} + Pt - H_{ads} \leftrightarrow Pt - OH_{ads} \tag{8}$$

The chemical oxidation of CO should be dominant in our case, as the potential of the CO electrooxidation should be higher than 0.4 V for the Pt catalyst at 60 °C [68,71,72], while the anode overpotentials for the samples investigated were 0.210 and 0.295 V under H_2/air operating conditions (Fig. 12). The H_2-crossover results support the hypothesis of a chemical conversion of CO to CO_2 because the smaller H_2-crossover value for the MEA 1 sample implies that the O_2 crossover was also reduced, leading to a higher anode overpotential, as depicted in Fig. 13.
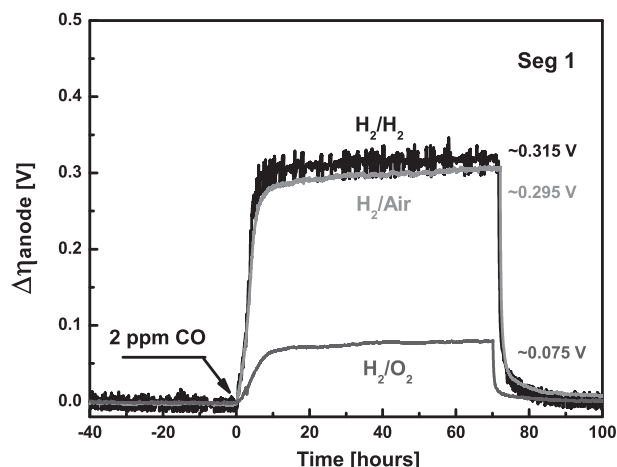

Fig. 13. Segment 1 transient anode overpotential for MEA 1 for a cell current of 0.8 A cm^{-2} and a 2 ppm CO exposure for the H_2/H_2, H_2/air, and H_2/O_2 gas configurations. Anode/cathode: 2/2 stoichiometry (or 0.847/0.847 l min^{-1}), 100/50 (or 100)% RH, 48.3/48.3 kPa$_g$, 60 °C.

The resulting impact of oxygen crossover on the oxidation of adsorbed CO on platinum has recently gained more importance due to the appearance of thinner membrane materials (from 180 to 25–15 μm) favoring oxygen crossover and thus CO catalytic oxidation. Such an effect also can be reached by an increase of only the cathode backpressure [73]. Oxygen diffusion through the membrane is considered to be the equivalent of an oxygen/air bleed (a few %) introduced into the H_2 reactant stream, a recognized CO poisoning mitigation method in addition to the application of Pt–Ru anode catalysts [73–75].

4. Conclusion

A segmented cell system was successfully applied to study the impacts of the fuel contaminant CO at a concentration of 2 ppm on fuel cell performance distribution. The effects of the cathode gas (O_2, air, H_2) and membrane permeability on the mitigation of CO impacts were also investigated. Upon the intentional injection of 2 ppm CO in to the hydrogen stream, the voltage decreased significantly during the initial 10 h, with voltage drops of 0.080, 0.300, and 0.320 V for O_2, air, and H_2 cathode gases, respectively. CO poisoning caused significant current redistribution in PEMFCs. Inlet segments 1–4 exhibited a significant decrease in current due to CO adsorption on Pt. In contrast, the outlet segments showed an increase in current. Spatial EIS data confirmed the dynamic responses of the segments upon CO exposure and revealed increases not only in HFR and anode charge transfer resistance but also in cathode charge transfer resistance for O_2 and air cathode gas configurations. Thus, CO also impacted the electrochemical processes at the cathode. The conversion of CO was assumed to proceed through a combination of catalytic and electrochemical oxidation reactions; however, the catalytic oxidation of CO is likely the dominant process. An increased membrane hydrogen permeability (which corresponds to an increased oxygen permeability) can mitigate the impact of CO, mainly due to the catalytic oxidation of adsorbed CO on the Pt anode by O_2. The cell voltage decrease under CO exposure was lower for MEA with a high hydrogen crossover current. The performance completely recovered within 1–2 h after CO injection stopped.

References

[1] L. Carrette, K.A. Friedrich, U. Stimming, Fuel Cells 1 (2001) 5–39.
[2] F. Laurencellel, R. Chahine, J. Hamelin, K. Agbossou, M. Fournier, T.K. Bose, A. Laperriere, Fuel Cells 1 (2001) 66–71.
[3] T. Susai, A. Kawakami, A. Hamadd, Y. Miyake, Y. Azegami, Fuel Cells Bull. 29 (2001) 7–11.
[4] J. Scholta, N. Berg, P. Wilde, L. Jörissen, J. Garche, J. Power Sources 127 (2004) 206–212.
[5] F. de Bruijn, Green Chem. 7 (2005) 132–150.
[6] M. Oszcipok, M. Zedda, J. Hesselmann, M. Huppmann, M. Wodrich, M. Junghardt, C. Hebling, J. Power Sources 157 (2006) 666–673.
[7] P. Agnolucci, Int. J. Hydrogen Energy 32 (2007) 4319–4328.
[8] L. Venturelli, P.E. Santangelo, P. Tartarini, Appl. Therm. Eng. 29 (2009) 3469–3475.
[9] S. Shimpalee, M. Ohashi, J.W. Van Zee, C. Ziegler, C. Stoeckmann, C. Sadeler, C. Hebling, Electrochim. Acta 54 (2009) 2899–2911.

[10] J.R. Rostrup-Nielson, K. Aasberg-Petersen, Steam reforming, ATR, partial oxidation: catalysts and reaction engineering, in: W. Vielstich, H.A. Gasteiger, A. Lamm (Eds.), Handbook of Fuel Cell − Fundamentals, Technology and Applications, Fuel Cell Technology and Applications. Part 1, vol. 3, John Wiley and Sons, Weinheim, 2003, pp. 159−176. (Chapter 14).
[11] F. Barbir, PEM Fuel Cells: Theory and Practice, Elsevier Academic Press, 2005.
[12] U. Stimming, H.F. Oetjen, V.M. Schmidt, F. Trila, J. Electrochem. Soc. 143 (1996) 3838−3842.
[13] J.J. Baschuk, X. Li, Int. J. Energy Res. 25 (2001) 695−713.
[14] T.E. Springer, T. Rockward, T.A. Zawodzinski, S. Gottesfeld, J. Electrochem. Soc. 148 (2001) A11−A23.
[15] X. Cheng, Z. Shi, N. Glass, L. Zhang, J. Zhang, D. Song, Zh.-Sh. Liu, H. Wang, J. Shan, J. Power Sources 165 (2007) 739−756.
[16] T.R. Ralph, M.P. Hogarth, Platinum Met. Rev. 46 (2002) 117−135.
[17] K. Ruth, M. Vogt, R. Zuber, Development of CO-tolerant catalysts, in: W. Vielstich, H.A. Gasteiger, A. Lamm (Eds.), Handbook of Fuel Cell − Fundamentals, Technology and Applications, Fuel Cell Technology and Applications. Part 1, vol. 3, John Wiley and Sons, Weinheim, 2003, pp. 489−496. (Chapter 39).
[18] SAE TIR J2719, Hydrogen Specification Guideline for Fuel Cell Vehicles, November 2005.
[19] J. Wu, X.Z. Yuan, H. Wang, M. Blanco, J.J. Martin, J. Zhang, Int. J. Hydrogen Energy 33 (2008) 1747−1757.
[20] X. Yuan, H. Wang, J.C. Sun, J. Zhang, Int. J. Hydrogen Energy 32 (2007) 4365−4380.
[21] L.C. Pérez, L. Brandão, J.M. Sousa, A. Mendes, Renew. Sustain. Energy Rev. 15 (2011) 169−185.
[22] J.R. Claycomb, A. Brazdeikis, M. Le, R.A. Yarbrough, G. Gogoshin, J.H. Miller, IEEE Trans. Appl. Supercond. 13 (2003) 211−214.
[23] Hong-Chang Yang, Jau-Han Chen, Shu-Yun Wang, Chin-Hao Chen, Jen-Tzong Jeng, Ji-Cheng Chen, Chiu-Hsien Wu, Shu-Hsien Liao, Herng-Er Horng, Tamkang J. Sci. Eng. 6 (2003) 9−18.
[24] K.-H. Hauer, R. Potthast, T. Wüster, D. Stolten, J. Power Sources 143 (2005) 67−74.
[25] S. Cleghorn, C.R. Derouin, M.S. Wilson, S. Gottesfeld, J. Appl. Electrochem. 28 (1998) 663−672.
[26] M. Schulze, E. Gülzow, St Schönbauer, T. Knori, R. Reissner, J. Power Sources 173 (2007) 19−27.
[27] J. Stumper, S.A. Campbell, D.P. Wilkinson, M.C. Johnson, M. Davis, Electrochim. Acta 43 (1998) 3773−3783.
[28] M. Noponen, T. Mennola, M. Mikkola, T. Hottinen, P. Lund, J. Power Sources 106 (2002) 304−312.
[29] P.C. Ghosh, T. Wüster, H. Dohle, N. Kimiaie, J. Mergel, D. Stolten, J. Power Sources 154 (2006) 184−191.
[30] Z. Liu, Z. Mao, B. Wu, L. Wang, V.M. Schmidt, J. Power Sources 141 (2005) 205−210.
[31] Ch Wieser, A. Helmbold, E. Gülzow, J. Appl. Electrochem. 30 (2000) 803−807.
[32] G. Bender, M.S. Wilson, T.A. Zawodzinski, J. Power Sources 123 (2003) 163−171.
[33] A.B. Geiger, R. Eckl, A. Wokaun, G.G. Scherer, J. Electrochem. Soc. 151 (2004) A394−A398.
[34] F.N. Büchi, A.B. Geiger, R.P. Neto, J. Power Sources 145 (2005) 62−67.
[35] J.J. Hwnag, W.R. Chang, R.G. Peng, P.Y. Chen, A. Su, Int. J. Hydrogen Energy 33 (2008) 5718−5727.
[36] Y.-G. Yoon, W.-Y. Lee, T.-H. Yang, G.-G. Park, Ch.-S. Kim, J. Power Sources 118 (2003) 193−199.
[37] I.A. Schneider, H. Kuhn, A. Wokaun, G.G. Scherer, J. Electrochem. Soc. 152 (2005) A2092−A2103.
[38] N. Rajalakshmi, M. Raja, K.S. Dhathathereyan, J. Power Sources 112 (2002) 331−335.
[39] D. Natarajan, T.V. Nguyen, AIChe J. 51 (2005) 2587−2598.

[40] M.M. Mench, C.Y. Wang, J. Electrochem. Soc. 150 (2003) A79−A85.
[41] H. Sun, G. Zhang, L.-J. Guo, Sh. Dehua, H. Liu, J. Power Sources 168 (2007) 400−407.
[42] F.-B. Weng, B.-Sh. Jou, Ch.-W. Li, A. Su, Sh.-H. Chan, J. Power Sources 181 (2008) 251−258.
[43] T.V. Reshetenko, G. Bender, K. Bethune, R. Rocheleau, Electrochim. Acta 56 (2011) 8700−8710.
[44] T.V. Reshetenko, G. Bender, K. Bethune, R. Rocheleau, Electrochim. Acta 69 (2012) 220.
[45] I.A. Schneider, S.A. Freunberger, D. Kramer, A. Wokaun, G.G. Scherer, J. Electrochem. Soc. 154 (2007) B383−B388.
[46] I.A. Schneider, D. Kramer, A. Wokaun, G.G. Scherer, J. Electrochem. Soc. 154 (2007) B770−B782.
[47] T.V. Reshetenko, G. Bender, K. Bethune, R. Rocheleau, Electrochim. Acta 76 (2012) 16.
[48] T. Reshetenko, G. Bender, R. Rocheleau, The Effect of Local Variations in the Gas Diffusion Layer Properties on Spatial PEMFC Performance, LDR35−47, 2009 Fuel Cell Seminar, November 16−20, 2009, Palm Springs, CA, USA.
[49] R. Lin, E. Gülzow, M. Schulze, K.A. Friedrich, J. Electrochem. Soc. 158 (2011) B11−B17.
[50] T. Murahashi, T. Mitsumoto, E. Nishiyama, ECS Trans. 25 (2009) 869−879.
[51] D.J.L. Brett, P. Aguiar, N.P. Brandon, A.R. Kucernak, Int. J. Hydrogen Energy 32 (2007) 863−879.
[52] T. Tingelöf, L. Hedström, N. Holmström, P. Alvfors, G. Lindbergh, Int. J. Hydrogen Energy 33 (2008) 2064−2072.
[53] M. Boaventura, H. Sander, K.A. Friedrich, A. Mendes, Electrochim. Acta 56 (2011) 9467−9475.
[54] G. Bender, M. Angelo, S. Dorn, K. Bethune, R. Rocheleau, Quantitative analysis of the impact of low level carbon monoxide exposure to proton exchange membrane fuel cells, J. Power Sources (in preparation).
[55] T.E. Springer, T.A. Zawodzinski, M.S. Wilson, S. Gottesfeld, J. Electrochem. Soc. 143 (1996) 587−599.
[56] J.M. Le Canut, R. Abouatallah, D.A. Harrington, J. Electrochem. Soc. 153 (2006) A857−A864.
[57] N. Wagner, E. Gülzow, J. Power Sources 127 (2004) 341−347.
[58] D. Chakraborty, I. Chorkendorff, T. Johannessen, J. Power Sources 162 (2006) 1010−1022.
[59] Y.-C. Liu, X.-P. Qiu, W.-T. Zhu, G.-S. Wu, J. Power Sources 114 (2003) 10−14.
[60] F. Hajbolouri, B. Andreaus, G.G. Schere, A. Wokaun, Fuel Cells 4 (2004) 160−168.
[61] X. Wang, I.-M. Hsing, Y.-J. Leng, P.-L. Yue, Electrochim. Acta 46 (2001) 4397−4405.
[62] Z. Qi, C. He, A. Kaufman, J. Power Sources 111 (2002) 239−247.
[63] M. Ciureanu, H. Wang, J. Electrochem. Soc. 146 (1999) 4031−4040.
[64] M.-C. Yang, Ch.-H. Hsueh, J. Electrochem. Soc. 153 (2006) A1043−A1048.
[65] J. Zhang, T. Thampan, R. Datta, J. Electrochem. Soc. 149 (2002) A765−A772.
[66] G.A. Camara, E.A. Ticianelli, S. Mukerjee, S.J. Lee, J. McBreen, J. Electrochem. Soc. 149 (2002) A748−A753.
[67] S. Jiménez, J. Soler, R.X. Valenzuela, L. Daza, J. Power Sources 151 (2005) 69−73.
[68] H.A. Gasteiger, N.M. Markovic, P.N. Ross, J. Phys. Chem. 99 (1995) 8290−8301.
[69] N.M. Markovic, T.J. Schmidt, B.N. Grgur, H.A. Gasteiger, R.J. Behm, P.N. Ross, J. Phys. Chem. B 103 (1999) 8568−8577.
[70] N.M. Markovic, C.A. Lucas, B.N. Grgur, P.N. Ross, J. Phys. Chem. B 103 (1999) 9616−9623.
[71] T. Ioroi, K. Yasuda, Y. Miyazaki, Phys. Chem. Chem. Phys. 4 (2002) 2337−2340.
[72] T. Gu, W.-K. Lee, J.W. Van Zee, Appl. Catal. B 56 (2005) 43−49.
[73] W. Wang, J. Power Sources 191 (2009) 400−406.
[74] S. Gottesfeld, J. Pafford, J. Electrochem. Soc. 135 (1988) 2651−2652.
[75] M. Murthy, M. Esayian, A. Hobson, S. MacKenzie, W.-K. Lee, J.W. Van Zee, J. Electrochem. Soc. 148 (2001) A1141−A1147.